International Journal of Hydrogen Energy 58 (2024) 1030–1043

Contents lists available at ScienceDirect

International Journal of Hydrogen Energy

journal homepage: www.elsevier.com/locate/he

Deep learning analysis of plasma emissions: A potential system for monitoring methane and hydrogen in the pyrolysis processes

Ali Salimian *, Enrico Grisan

School of Engineering, London Southbank University, 103 Borough Road, London, SE1 0AA, UK

ARTICLE INFO

Handling Editor: Jinlong Gong

Keywords:
Monitoring
Plasma
Deep learning
Pyrolysis
Methane
Hydrogen

ABSTRACT

The estimation of methane and hydrogen production as output from a pyrolysis reaction is paramount to monitor the process and optimize its parameters. In this study, we propose a novel experimental approach for monitoring methane pyrolysis reactions aimed at hydrogen production by quantifying methane and hydrogen output from the system. While we appreciate the complexity of molecular outputs from methane hydrolysis process, our primary approach is a simplified model considering detection of hydrogen and methane only which involves three steps: continuous gas sampling, feeding of the sample into an argon plasma, and employing deep learning model to estimate of the methane and hydrogen concentration from the plasma spectral emission. While our model exhibits promising performance, there is still significant room for improvement in accuracy, especially regarding hydrogen quantification in the presence of methane and other hydrogen bearing molecules. These findings present exciting prospects, and we will discuss future steps necessary to advance this concept, which is currently in its early stages of development.

1. Introduction

The concept of a hydrogen-based economy revolves around the utilization of hydrogen as a viable source of fuel [1]. Hydrogen stands out as a highly promising energy carrier, renowned for being an exceptionally clean fuel since its combustion results solely in the production of water. Furthermore, when compared to traditional fossil fuels, hydrogen shows a higher energy yield per unit mass, underlining its potential significance [2,3].

Hydrogen has garnered significant attention, primarily for its applications in fuel cells and internal combustion engines, thereby paving the way for the establishment of a low-carbon hydrogen economy. One of its key advantages lies in the efficient conversion of hydrogen's chemical energy into electricity and various other energy forms, all accomplished without the emission of greenhouse gases [4,5]. Moreover, hydrogen plays a pivotal role in the formulation of innovative approaches to transform industrial CO2 emissions into valuable platform chemicals, representing a significant step toward sustainability.

1.1. Hydrogen production

Approximately 96 % of global hydrogen production, as per current data [6], is obtained through methods such as coal gasification, oil/-naphtha reforming, and steam methane reforming (SMR). Nevertheless, these processes have a profound environmental impact due to the significant volume of CO2 emissions they generate (Fig. 1). illustrates the CO2 footprint associated with various hydrogen production techniques [7].

While SMR has a high energy efficiency of ~75 %, it is undermined for its reliance on a carbon capture and storage system which simply translates to cost and potentially high carbon fottprint.

Furthermore, the conventional methods designed for Carbon Capture and Storage (CCS) incur a substantial environmental footprint due to their elevated electricity consumption, which further amplifies the overall environmental impact of the process [8,9].

Significant efforts are currently underway to establish industrial strategies for hydrogen production while minimizing CO2 emissions. Two emerging technologies in this regard are thermochemical water splitting and water electrolysis [10,11], both of which yield hydrogen and oxygen as their sole products.

Water electrolysis involves the decomposition of water into oxygen and hydrogen through the passage of an electric current. The production of hydrogen from water via electrolysis represents a completely carbon dioxide-free alternative, provided that the electricity required is sourced exclusively from renewable resources. However, it's important to note

* Corresponding author.
E-mail address: salimiaa@lsbu.ac.uk (A. Salimian).

https://doi.org/10.1016/j.ijhydene.2024.01.251
Received 22 October 2023; Received in revised form 18 January 2024; Accepted 20 January 2024
Available online 31 January 2024

List of abbreviations

GHG	Greenhouse gases
SMR	Steam methane reforming
CCS	Carbon capture system
CNN	convolutional neural networks
ppm	Parts per million

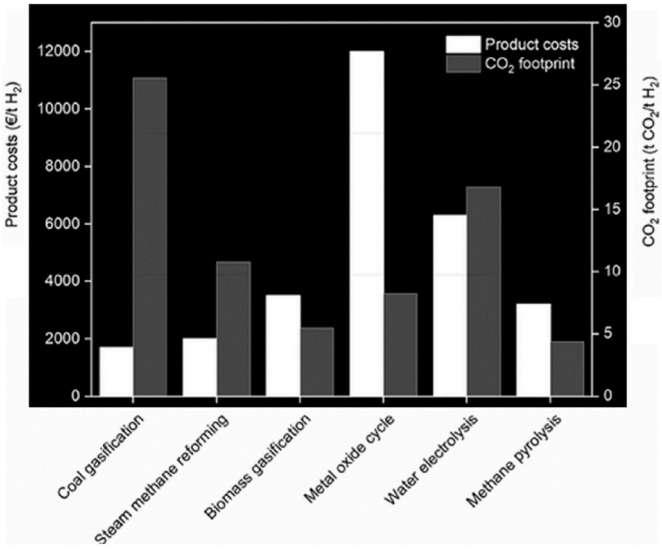

Fig. 1. Cost vs CO2 footprint of various hydrogen production techniques [7].

that if the electricity used is not 100 % emissions-free, water electrolysis can surpass the carbon footprint of SMR due to its high energy demands [10].

Thermochemical water splitting primarily employs redox-active metal oxide cycles, a method that necessitates exceptionally high temperatures (exceeding 1300 °C), which can be achieved through large-scale solar concentration systems. This technology capitalizes on two essentially limitless resources, namely water and sunlight. The integration of solar energy concentration systems with water-splitting structures holds vast potential for transforming the energy landscape and bolstering the economy. Presently, this process faces challenges in terms of its industrial viability due to relatively low efficiency and substantial processing costs. When subject to economic evaluation for large-scale hydrogen production, the metal oxide cycle emerges with the highest product costs and demands a substantial investment [7].

On the other hand, another possible source of hydrogen is represented by methane, the primary constituent of natural gas, that stands out as an abundant and readily available raw material, thanks to the vast reservoirs of natural gas. However, as (SMR) is associated with substantial carbon dioxide (CO2) emissions, there is a pressing need to explore cleaner alternatives. One promising option is the thermal decomposition of methane, commonly referred to as methane pyrolysis. This process offers a viable alternative since it yields only hydrogen and solid carbon as reaction products, effectively preventing the generation of CO2 during the reaction itself [5].

Methane pyrolysis offers the advantage of being a one-step process, unlike (SMR), which requires an additional Water-Gas Shift (WGS) reaction. The WGS reaction serves to convert the carbon monoxide (CO) produced during the methane and water reaction into carbon dioxide (CO2) while producing extra hydrogen [12].

In terms of energy efficiency, SMR outperforms methane pyrolysis when carbon dioxide sequestration via a carbon capture system (CCS) is not considered, boasting a higher efficiency rate (75 % compared to 58 %). However, when factoring in the implementation of CCS systems, the net energy efficiency of both processes becomes quite similar, with SMR achieving 60 % efficiency and methane pyrolysis reaching 58 % [13].

Methane pyrolysis technology offers a compelling advantage in the production of hydrogen, combining cost-effectiveness with low or near-zero emissions. When compared to direct combustion, natural gas pyrolysis has the potential to be significantly more efficient in reducing greenhouse gas (GHG) emissions [14,15].

In terms of emissions, alternative methane conversion technologies exhibit certain limitations. For instance, the (SMR) process yields 0.5 kg of hydrogen per kilogram of methane and emits 9–12 kg of carbon dioxide equivalent per kilogram of hydrogen [16]. One of the primary merits of methane pyrolysis is its capacity to produce hydrogen gas with a noteworthy 75 % reduction in GHG emissions compared to the SMR process (resulting in 2–3 kg of CO2 per kilogram of hydrogen when natural gas serves as the heat source).

Additionally, the solid carbon byproduct generated through methane pyrolysis can take on various forms, ranging from amorphous carbon black to well-structured graphitic materials and even specialized carbon nanotubes and fibres. The value and pricing of the solid carbon are determined by its specific characteristics and grade, thereby creating the potential for generating additional revenue through the production of high-value carbon products [17]. However, this topic needs further considerations by experts in the field with respect to the quantitative market demand for carbon black products and the carbon black output via methane pyrolysis.

The thermal decomposition of methane is an endothermic chemical reaction that necessitates temperatures exceeding 900 °C [18]. This process is also susceptible to various influencing factors, including pressure and the presence of catalysts.

Alterations in the pressure of the methane pyrolysis reaction, especially at its thermodynamic equilibrium state, adhere to Le Chatelier's principle (states that when you change conditions for a chemical reaction at equilibrium, the system will adjust to counteract that change and restore equilibrium. This applies to changes in concentration, pressure for gases and temperature); resulting in reduced methane conversion and hydrogen yield. However, under real operating conditions that deviate from equilibrium, elevated reaction pressure decreases the rate of methane conversion but increases the quantity of reactants within the reactor. Consequently, this leads to a higher production of hydrogen. To achieve economically competitive results, it is crucial for the methane pyrolysis reactor to operate at an optimal pressure that balances desirable methane conversion rates with energy efficiency.

Solid catalysts can be employed to lower the requisite temperature for the process. Enhanced methane conversion rates correspond to increased rates of hydrogen and carbon production. During this process, carbon particles may deposit on the surface of the solid catalyst and migrate through it, which eventually leads to the deactivation of active catalyst sites over time [19,20]. Consequently, the rate of hydrogen production is influenced by catalyst deactivation, and the recovery of the catalyst presents a costly endeavour.

Without a solid catalyst, methane pyrolysis demands temperatures exceeding 1000 °C to achieve a substantial hydrogen yield. These elevated temperatures are essential due to the formidable and stable carbon-hydrogen (C–H) bonds found within symmetrical methane molecules [21].

To mitigate the need for such high temperatures, researchers have developed both metal (such as Fe, Ni, Co) and non-metal (carbon) catalysts. These catalysts serve the purpose of reducing the reaction temperature and enhancing the rate of methane conversion [22].

Research by Plevan et al. [23] and Geißler et al. [24] has highlighted the potential use of molten tin (Sn) and lead (Pb) to generate hydrogen and separable carbon through the methane pyrolysis reaction. However, their pyrolysis activities were found to be relatively low when compared

to other molten metals like Ni–Bi or Cu–Bi alloys.

Subsequent studies by Palmer et al. [25] and Chester et al. [26] indicated that Ni–Bi and Cu–Bi alloys could significantly enhance the methane conversion rate in comparison to using molten bismuth (Bi) alone as the medium. Meanwhile, Serban et al. [27] explored the performance of mixtures involving molten Sn and silicon carbide (SiC) as catalysts for methane pyrolysis. It's worth noting that carbon produced via molten metal and salt systems may contain impurities from the metal and salt that are challenging to separate [28].

In addition to molten metals, molten salts have also been employed in methane pyrolysis, particularly transition metal halides and alkali halides that remain stable under reducing conditions [29]. Rahimi et al. [28] employed an immiscible mixture of molten salt and metal to enhance the purity of the solid carbon. Kang et al. [29,30] demonstrated that transition metal halides, such as manganese chloride (MnCl2) and iron chloride (FeCl2), exhibit high activity in the methane pyrolysis process.

To address the challenges associated with methane pyrolysis, researchers have developed various reactor systems and explored alternative thermal sources [31]. A comprehensive report on these systems and details of the hydrolysis process are reviewed by Patlolla et al. and Bastardo et al. [32,33].

1.2. Methane detection and quantification

Everything discussed so far in section 1.1 indicates the importance of being able to monitor and observe the reaction leading to hydrogen generation in a real time when industrial scale productions is considered. Irrespective of what system is to be implemented, ultimately at some point the efficiency of the hydrogen production needs to be assessed by monitoring the concentration of output hydrogen and possible leaking of the methane into the output gas if 100 % conversion is not achieved.

In terms of methane detection, currently there are existing technologies available in the market, which can be considered:

Optical sensors operate by detecting alterations in light waves stemming from interactions between the analyte and the receptor component. These sensors offer a non-destructive means of analysis, remain impervious to electromagnetic interference, and can function in environments devoid of oxygen. However, it's essential to acknowledge certain limitations associated with optical sensors, including their relatively high cost, substantial power consumption, and the challenge of achieving significant and distinctive results within the optical absorption region specific to methane [34–37].

Calorimetric sensors function by quantifying the heat generated during a reaction and then establishing a correlation with the concentration of the reactant. These sensors come with several advantages, such as being cost-effective, featuring a straightforward design, portability, ease of manufacture, and robust selectivity for methane. They can also perform reliably in challenging environmental conditions. However, it's important to acknowledge some of the drawbacks associated with calorimetric sensors, including their limited detection accuracy, vulnerability to issues like cracking, catalyst poisoning, and oversaturation, high power consumption, relatively short lifespan, and the necessity for operating at elevated temperatures [38–41].

Pyroelectric sensors operate by converting thermal energy into electrical energy, exploiting the phenomenon of pyroelectricity. These sensors offer several advantages, including non-destructiveness, the ability to function without the presence of oxygen, good sensitivity, high responsivity, a wide measuring range, and operation at room temperature. However, it's worth noting that pyroelectric sensors come with certain limitations, such as their relatively high cost, significant power consumption, immobility, and the challenges associated with their manufacturing process [42–44].

Semiconducting metal oxide sensors operate by detecting changes in conductivity resulting from the gas's absorption on the surface of a metal oxide. These sensors offer several advantages, including affordability, lightweight and robust construction, a long lifespan, and resistance to poisoning. However, there are certain limitations associated with semiconducting metal oxide sensors, including poor selectivity, a relatively small and narrow operational temperature range, a slow recovery rate, significant dependence on additives, sensitivity to temperature fluctuations, susceptibility to degradation, and responsiveness to changes in humidity [45–48].

Electrochemical sensors offer a versatile means of quantifying target gas concentrations by initiating either oxidation or reduction reactions at an electrode and subsequently measuring the resultant electrical current. These sensors come in various forms, each with its unique advantages and drawbacks. Amperometry (AE) sensors, for instance, provide affordability but are susceptible to issues like leakage, evaporation, and slow response times due to their use of hazardous materials. Ionic Liquid (IL) sensors, on the other hand, employ non-hazardous materials and demonstrate good selectivity for gases like methane while being able to detect even minor leaks. Solid Electrolyte (SE) sensors stand out for their leak-proof design, safety, robustness, and sensitivity to small leaks, yet they require elevated temperatures for operation and may struggle with low gas concentrations or potential degradation of the electrolyte. Each type caters to specific needs but necessitates a careful consideration of their respective advantages and limitations in practical applications [49–51].

Gas chromatography, (GC) boasts several advantages, including exceptional accuracy, resistance to interference, visualization capabilities, and adaptability for a variety of applications. A typical GC system consists of five crucial components: the carrier gas system, injector, separator (column oven), detector, and workstation. Within the GC system, the components present in the injected sample undergo separation within the column. This separation process enables the simultaneous and rapid quantitative analysis of the various compositions within the sample. As a result, GC has found extensive application in multicomponent analysis across diverse fields, including petroleum, chemical and biological engineering, environmental protection, and more. Its capacity to analyse complex mixtures makes swiftly and accurately it an invaluable tool in various scientific and industrial endeavours [52].

Recently, with the emergence of advanced computing and machine learning algorithms, some researchers have attempted to detect trace methane levels with plasma optical emission spectroscopy [53]. In this study, researchers conducted an analysis of emission spectra emanating from a radio frequency cold atmospheric plasma generated using helium and methane. They employed a low-cost and low-resolution spectrometer to capture spectra across three independent experimental runs, each featuring varying methane (CH4) concentrations ranging from 0 ppm to 100 ppm. Additionally, the model's robustness and recovery capabilities were put to the test during and after methane saturation events, involving concentrations as high as 20,000 ppm.

The analysis of these spectra adopted a data-driven approach with the objective of detecting methane concentrations at or above 2 parts per million (ppm). The results revealed an initial accuracy of 86 %, which was further improved to 96 % through the application of a custom alignment procedure. This research showcases a promising method for precisely and reliably detecting methane at low concentrations, holding significance for various applications requiring sensitive gas detection [53].

1.3. Proposed methane monitoring system

In this study we propose a monitoring system based on frequent sampling of the product gas from a column reactor. Fig. 2 illustrates a representative molten metal/salt pyrolysis reactor, together with an example of how coupling with the proposed system for methane/hydrogen quantification. The flow of the output gas into the system is controlled via a Mass Flow Controller (MFC) unit which are commercially available and operates on the principle of thermal mass flow

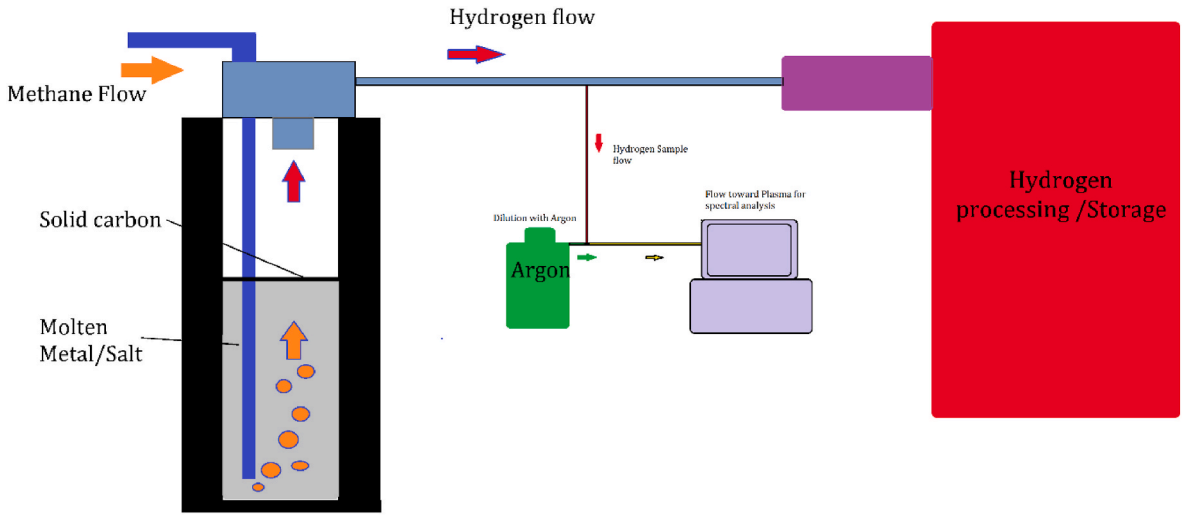

Fig. 2. Conceptual illustrative example of where our detection system will be placed for analysis. The hydrogen output from the column reactor is diluted with argon and is fed into a small plasma chamber for spectral analysis of the plasma. The flow of the input gas to the system can be controlled via a (MFC) device.

measurement to precisely regulate the flow rate of gases in various industrial processes. The key components include a flow sensor, typically a heated element, and a temperature sensor. The MFC maintains a constant temperature differential (CTD) between the heated element and the gas flow. As the gas flows over the heated sensor, the amount of heat required to maintain the CTD is directly proportional to the flow rate. The MFC incorporates a control valve that adjusts the flow by regulating gas pressure or altering the flow path. Operating within a closed-loop control system, the MFC continuously measures the actual flow rate and adjusts the control valve to maintain the desired setpoint. Communication interfaces enable integration into larger control systems, facilitating remote monitoring and control. MFCs find extensive use in semiconductor manufacturing, gas chromatography, research laboratories, and industrial processes requiring precise and stable control of gas flows. Calibration for specific gases ensures accurate performance tailored to the application's requirements.

The image illustrated in Fig. 2 represents a simplified presentation of a future prosed concept, however in reality during methane hydrolysis processes, the potential presence of impurities can stem from various sources, including the feedstock and reactor conditions. Depending on the purity of the methane feedstock, trace hydrocarbons may be present, alongside by-products such as carbon monoxide (CO) and carbon dioxide (CO2) resulting from incomplete hydrolysis or side reactions. Water vapor (H2O) is a natural by-product of the hydrolysis process. Additionally, methane decomposition under certain conditions can yield various carbon-containing species. The specific impurity composition is influenced by factors like process parameters, catalysts used, and feedstock quality. Purification steps are commonly employed to eliminate impurities and obtain a high-purity hydrogen product. Careful control of process conditions is essential to minimize the formation of undesired by-products and impurities. Based on the setup illustrated in Fig. 2, the spectral data captured from the plasma in real time will be constantly evaluated by deep learning model, trained on similar spectral data associated with known quantities of hydrogen and methane.

2. Materials and method

It is imperative to underscore that the experiments presented in this article are deliberately simplified and focused on the introduction of hydrogen and methane into the monitoring system. The primary objective is to explore the capability of our technique for the quantification of these specific gases. Acknowledging that in a real-life scenario, with the potential presence of various other molecules, further efforts are anticipated to involve enhanced data collection, as well as rigorous model training and testing. This strategic approach ensures a systematic and thorough investigation into the broader applicability of the proposed methodology, laying the groundwork for future comprehensive studies.

The experiments were carried out by modifying a small radio frequency plasma generator with a cylindrical chamber. An optical collimator was fitted on the chamber to capture the spectral emissions of the plasma and guide it via a quartz optical fibre into a spectrometer. The plasma generator is capable of intaking three different gasses via three independent mass flow controllers for precise injection of the required gas into the chamber.

In our experiments, the machine was connected to a source of Argon, Methane and a 5 % (Hydrogen/Argon mix) source. The plasma was generated via a constant 120w of RF energy. The set up of our prototype is illustrated in (Fig. 3).

By varying the flow rates of the three gas inputs, we can obtain an input mix with a varying range of ppm of methane and hydrogen, from pure argon to different mixed ratios of the three gasses. The concentration of both gases in the plasma chamber was capped at ~5 % in terms of square cubic centimetre per minute (sccm) flow rate compared to pure argon flow rate.

The data were captured at various flow rates selected on random basis over a timespan of four days ensuring that the plasma generator was switched on an off in between the days. This was done so to provide significant random approach toward our data collection.

For each plasma condition associated with certain methane or hydrogen content, between 10 and 20 spectral data points were collected with an integration time of 100 ms.

The spectral emissions in their raw form are an array of intensity values associated with emissions observed by the spectrometer starting at wavelength of 200 nm–1100 nm with 0.2 nm resolution. The emission intensity at each wavelength is associated with photons emitted during electronic transition of a particular atom or molecule present in the plasma. These transitions are related to various states of argon atoms or ions, hydrogen molecules or ions and methane derivatives. As such the spectral array can resemble a soup of numerous hidden data points that hold information on ingredients of the plasma and their quantity.

The objectives of these experiments have been to generate a large data bank of plasma spectrums associated with various rations of argon, hydrogen, and methane. In the next step, we developed a deep neural network that can learn precise quantitative atomic or molecular presence from these spectral data.

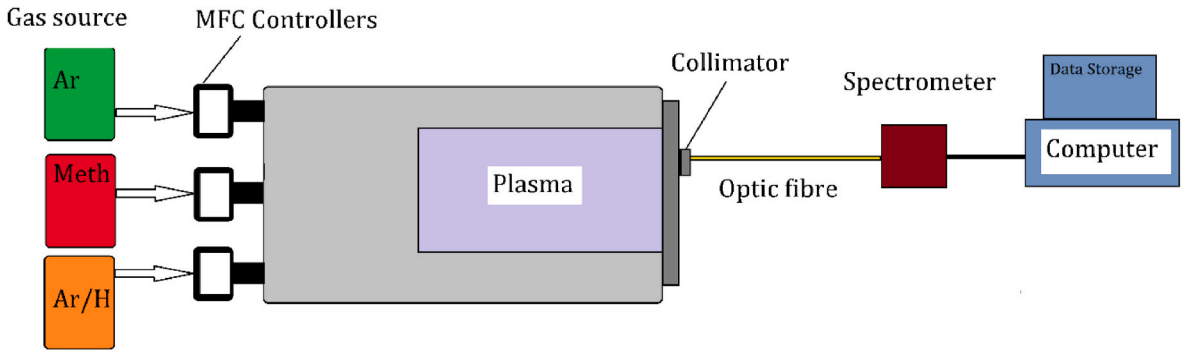

Fig. 3. Experimental set up. The plasma unit was fed with three separate gases via three separate MFC controllers. By varying the ratio of the gas input (min flow rate of 0.1 sccm) numerous spectral emission data from the plasma was captured and stored.

Upon training the model with spectral data associated with exactly known quantity of atomic/molecular presence we test the model by evaluating its performance on calculating the atomic content of the plasma from a set of spectral data that it has not been exposed to previously.

Overall, a total of four thousand nine hundred and seventy-five (4975) spectral data were collected. Of this data, some were associated with only argon without any hydrogen or methane resembling a spectrum associated to only argon. Some were associated with argon and hydrogen; some were associated with argon and methane and finally some contained all three gases in the plasma. The distribution of the spectral data in accordance with the gas content is presented in (Fig. 4). Taking a data science approach, this distribution of the data points would be considered unbalanced as we can see for example the number of data points associated with only hydrogen present in the plasma are higher than other conditions. Data scientists would conventionally prefer a balanced distribution of the data, however in these experiments, because our main objective is to prove a concept at a very early stage, we intentionally tried to maximise randomness in our approach toward data collection.

Regarding imbalanced datasets in regression, while the term "imbalanced" is more commonly associated with classification problems, it can apply to regression scenarios where there's a significant skew in the distribution of target values. In such cases, deep learning models can still be beneficial. They can capture the nuances of both the majority and minority target values, enabling better predictive performance across the entire range of the target variable. Careful consideration of data preprocessing, loss functions, and evaluation metrics tailored to regression problems will help leverage the potential advantages of deep learning when dealing with imbalanced datasets in this context. As such, preparing a well-balanced dataset was not our objective; rather, the objective was to prove the concept using a challenging dataset.

In terms of the actual parts per million (ppm) contents of each gas present in the argon plasma, we tried to take the same approach and make it as random as possible. Given the limitation of our mass flow controllers feeding the gas into the plasma which was at 0.1 square cubic centimetre per minute and our source gas concentrations we could achieve the following minimum values; Minimum hydrogen content 62 ppm and we went to a maximum of 50,000 ppm. With regards to methane the min methane content we tested was ~1230 ppm and maximum of 41,970 ppm. The distribution of the hydrogen and methane contents are presented in (Fig. 5).

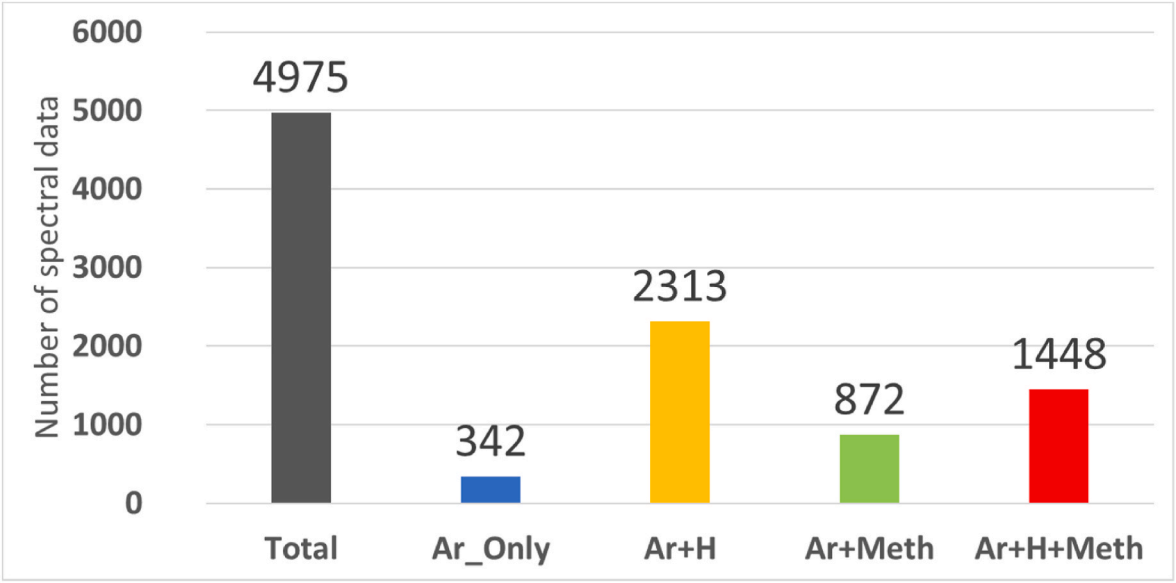

Fig. 4. The total number of spectral data and their association with the gas content. Argon only indicates no hydrogen or methane. This visualization delineates the distribution of spectral data across different gas compositions, including Argon only, Argon and Hydrogen, Argon and Methane, and a mix of Argon, Hydrogen, and Methane. Assessing the balance in these scenarios is pivotal for optimizing model training, ensuring a diverse dataset that enhances the model's adaptability to various gas combinations.

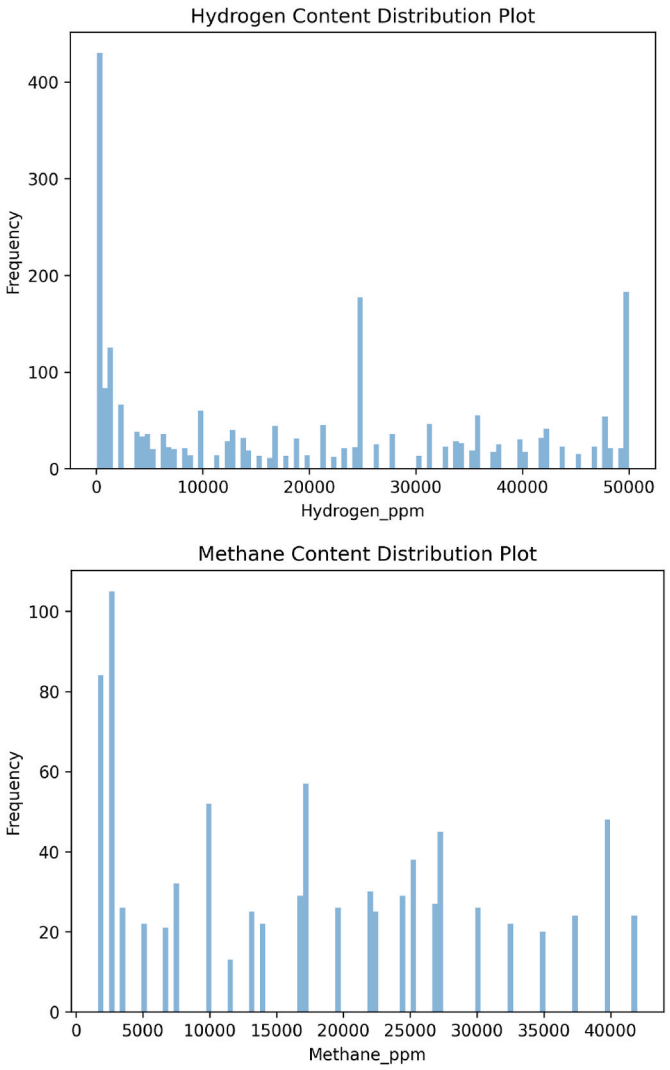

Fig. 5. The distribution frequency of hydrogen and methane contents in the plasma. Minimum hydrogen content was 62 ppm and minimum methane content was 1,663 ppm.

3. Theory and calculations

3.1. The deep learning model

Our deep learning model is based on the residual network structure that was originally developed by Kaiming He [54] as a deep residual learning for image recognition.

ResNet-50, short for Residual Network with 50 layers, represents a pivotal advancement in deep convolutional neural networks (CNNs) that has revolutionized image recognition and computer vision tasks. At its core, ResNet-50 utilizes residual blocks as its fundamental building blocks. These residual blocks address the vanishing gradient problem encountered when training extremely deep networks. Instead of striving to learn the underlying mapping directly, as in conventional networks, ResNet-50 introduces shortcut connections or skip connections within each residual block. These skip connections allow the network to learn residual functions—deviations from the identity mapping—making it easier to optimize the training process. By stacking multiple residual blocks, ResNet-50 creates a deep architecture while maintaining tractable training. The ResNet-50 architecture consists of five stages, contributing to the network's capacity to capture intricate patterns and high-level features in input images. The original ResNet50 was tailored and trained for identifying image content (computer vision classification), thus we modified the output layer to make the model adaptable for regression analysis rather than a classification task. The remarkable depth of ResNet-50, with its 50 layers, allows it to excel in various computer vision tasks, including image classification, object detection, and segmentation, achieving state-of-the-art performance. Its ingenuity lies in the ability to train deeper networks with increased accuracy, thus making ResNet-50 an indispensable tool in modern deep learning for image analysis.

Additionally the model is designed to take as input images which are technically 2D tensors. However, the spectral data obtained from the spectrometer is a single array (a 1D tensor). As such our single array spectral data must be converted into 2D tensors prior to model training. In order to reshape the spectral data into a 2D tensors, we trimmed the spectrum so to have 4500 data points. For simplicity we illustrate the process of single array to 2D conversion in (Fig. 6) where an array for length 24 is converted into a tensor of size (6 x 4). It's important to ensure that the final matrix dimension needs to be a multiple of the single array's size. Hence, we trimmed our single arrays so that data points from 195 nm to 1105 nm were selected at 0.2 nm resolution. This means every single array of our data contained 4500 data points and as such they were converted to 2D tensors of shape (50 x 90).

Once the arrays are converted into 2D tensors they can be used for training the model. While the ResNet-50 takes a complex set of procedures during the image processing, fundamentally two main processes are vital during model training; the images undergo numerous convolution and pooling steps. A very simplified representation of the model training steps is presented in (Fig. 7), however the actual model we used is significantly more complex than the illustration and reflects the original ResNet-50, except that the output neuron is modified to output a single number for complex regression analysis rather than a classification.

The following steps are carried out in our model's algorithm.

3.1.1. Convolution process

In deep convolutional neural networks (CNNs), the convolution process is a fundamental operation that plays a pivotal role in extracting meaningful features from input data, typically images. Convolution involves the use of small, learnable filters or kernels to scan the input data. These kernels slide over the input image in a systematic manner, computing a weighted sum of pixel values within their receptive fields. The key idea is that these learned kernels act as feature detectors, detecting specific patterns or features such as edges, textures, or shapes. During the convolution operation, the kernel's weights are shared across the entire input, which significantly reduces the number of parameters compared to fully connected layers. This parameter sharing property makes CNNs computationally efficient and capable of learning hierarchical representations of features. In essence, the convolution process gradually transforms the input image into a set of feature maps. Each feature map represents the response of one kernel to a specific feature in the input. By stacking multiple convolutional layers, the network can capture increasingly complex and abstract features, enabling it to recognize intricate patterns in the data. Mathematically convolution process can be described as such:

$$C[i,j] = \sum_{m=0}^{M-1} \sum_{n=0}^{N-1} I[i+m, j+n] \bullet K[m,n]$$

where C[i,j] is output feature map value at position [i,j], I is the input feature map, K is the filter and m and n are the dimensions of the filter.

3.1.2. Max-pooling process

Max-pooling is another crucial operation in CNNs that contributes to feature extraction and spatial dimension reduction. After each convolutional layer, max pooling is often applied to the feature maps. Max-pooling involves dividing the feature map into non-overlapping regions (typically 2x2 or 3x3 grids) and selecting the maximum value from each

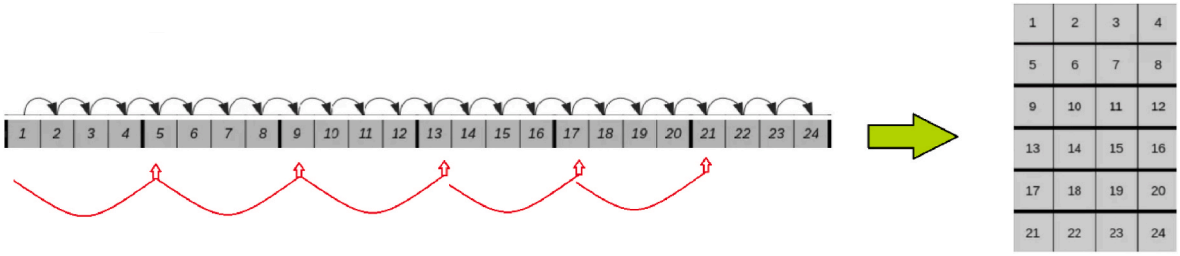

Fig. 6. The process of converting a single array into a 2D tensor.

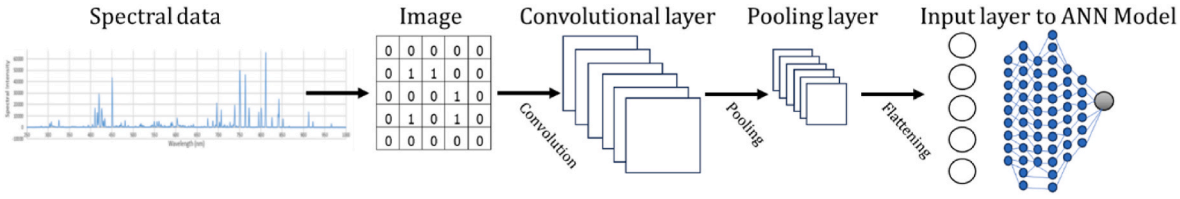

Fig. 7. A simple representation of training a CNN model with our spectral data.

region, discarding the rest. This process effectively reduces the spatial dimensions of the feature maps, down sampling the information. Max-pooling serves multiple purposes. Firstly, it enhances the network's translation invariance, making it more robust to small shifts and distortions in the input data. Secondly, it reduces the computational burden by reducing the number of parameters and the spatial dimensions, which is especially important in deep networks. Thirdly, max pooling helps to focus on the most salient features by retaining only the strongest activations in each region. In summary, convolution and max pooling are integral processes in CNNs that enable the network to automatically learn and extract hierarchical features from raw input data, facilitating the network's ability to perform complex tasks such as image classification, object detection, and segmentation in various scientific applications. The pooling process can be described as follows:

$$P[i,j] = \max_{m,n} I[i+m, j+n]$$

3.1.3. Artificial-neural network stage

Ultimately the output of the above steps is then converted into a single array which is fed to the artificial neural network part of the model. During the training of a neural network using the Mean Squared Error (MSE) loss function and the Adam optimizer, a series of crucial processes unfold. Initially, network weights and biases are randomly initialized. In each training epoch, input data is forwarded through the network, generating predictions (of methane or hydrogen content). Subsequently, the MSE loss function calculates the average squared difference between these predictions and the actual target values, serving as a measure of the network's performance on the training data. The backpropagation algorithm computes gradients of the loss with respect to network parameters, indicating the direction and magnitude of necessary adjustments. The Adam optimizer utilizes these gradients to efficiently update the weights and biases, optimizing the network's performance. This iterative process continues for a set number of epochs, with ongoing monitoring and validation to ensure generalization to new data. The final trained model is saved for future predictions on unseen data. Ultimately, this combination of MSE loss and the Adam optimizer is highly effective for regression tasks, enabling neural networks to learn and predict continuous values while minimizing the mean squared error between predictions and true values.

3.1.4. Optimization algorithm

We used the Adaptive Movement Estimation (Adam) optimizer for stochastic gradient descent algorithm to adjust the weights of the neural connections. The Adam optimization algorithm combines the benefits of both the Momentum and Root Mean Square Propagation (RMSP) gradient descent methods [55,56]. The key equations in the Adam algorithm involve the update of the moving averages, the bias correction step, and the weight update step.

The momentum method is an optimization algorithm that takes into consideration the exponentially weighted average and accelerates the gradient descent.

The weight at time t+1 is given by:

$$w_{t+1} = w_t - \alpha \bullet m_t$$

where α is the step size or learning rate, the hyperparameter that controls how far to move in the search space against the gradient each iteration of the algorithm and m_t is the aggregate of gradients at current time t (initially, 0), given by:

$$m_t = \beta m_{t-1} + (1-\beta)\left[\frac{\partial L}{\partial w_t}\right]$$

Where m_{t-1} is the aggregate of gradients at current time t-1 (previous), β is a moving average parameter, ∂L is the derivative of Loss Function and ∂w_t is the derivative of weights at time t.

RMSP is an adaptive learning algorithm and an improved version of AdaGrad. Instead of taking the cumulative sum of squared gradients like in AdaGrad, it takes the exponential moving average.

The weight at time t+1 is given by:

$$w_{t+1} = w_t - \frac{\alpha}{\sqrt{v_t + \varepsilon}}\left[\frac{\partial L}{\partial w_t}\right]$$

where ε is a small positive constant (added to avoid division by 0) and v_t is the sum of square of past gradients at time t (initially, Vt = 0), given by:

$$v_t = \beta v_{t-1} + (1-\beta)\left(\frac{\partial L}{\partial w_t}\right)^2$$

Taking the equations used in the both optimizers, we get:

$$m_t = \beta_1 m_{t-1} + (1-\beta_1)\left[\frac{\partial L}{\partial w_t}\right]$$

$$v_t = \beta_2 v_{t-1} + (1-\beta_2)\left(\frac{\partial L}{\partial w_t}\right)^2$$

Where β_1 and β_2 are the decay rates of average of gradients in each method with values ≈ 1.

Since m_t and v_t have both initialized as 0, both tend to be biased towards 0, as both $\beta 1$ & $\beta 2 \approx 1$. Adam optimizer corrects this problem by computing bias-corrected m_t and v_t. The equations are as follows:

$$\widehat{m}_t = \frac{m_t}{1 - \beta_1^t}$$

$$\widehat{v}_t = \frac{m_t}{1 - \beta_1^t}$$

Introducing this the bias-corrected weight parameters in the original equation we get:

$$w_{t+1} = w_t - \alpha\left(\frac{\widehat{m}_t}{\sqrt{\widehat{v}_t + \epsilon}}\right)$$

The algorithm effectively adapts the learning rates of individual parameters by considering both the first moment (mean) and the second moment (uncentered variance) of the gradients. This helps the optimizer converge faster and handle different scales of gradients in different dimensions.

3.1.5. Learning rate

In deep learning, the learning rate is a critical hyperparameter that determines how much a neural network's weights should be adjusted during training. It plays a pivotal role in the optimization process, affecting the speed and stability of convergence. A large learning rate can lead to faster convergence but may risk overshooting the optimal solution or causing instability. On the other hand, a small learning rate provides stability but may result in slow convergence. Selecting an appropriate learning rate often involves experimentation and hyperparameter tuning to find the balance between rapid convergence and steady progress towards an optimal model. The choice of learning rate significantly influences the training effectiveness and final performance of deep neural networks.

3.1.6. Training epoch

In deep learning, a training epoch is a complete pass through the entire training dataset during the training phase of a neural network. It represents one iteration of the training process, where the model makes predictions on all the training examples, computes the loss (error) between the predicted values and the actual targets (labels), and updates the model's parameters (weights and biases) to minimize this loss.

We conducted multiple epochs. In each epoch, the entire training dataset is used to update the model's parameters, and this process is repeated for a predefined number of epochs or until a certain convergence criterion is met. Increasing the number of training epochs can lead to better model performance, but it can also risk overfitting the model to the training data. Therefore, finding the right balance between the number of epochs and model generalization is a crucial part of training deep neural networks.

3.2. Model training

As discussed previously all the spectral data were converted into 2D tensors of shape (50,90). Prior to model training, all the training 2D tensors were also normalised using min max scaling which is represented below:

$$\mathrm{x(min\ \ maxscaled)} = \frac{x - \min(x)}{\max(x) - \min(x)}$$

Normalization is a crucial step in the realm of deep learning, offering numerous advantages that enhance the training process and the performance of neural networks. Firstly, it ensures stability and accelerates convergence, mitigating the risk of slow training or non-convergence that may occur when input features have varying scales. Secondly, normalization contribute to improved gradient flow within the network. This is vital for avoiding issues like vanishing or exploding gradients, which can severely hinder the training of deep neural networks. Lastly, normalization serves as a regularization technique, aiding in preventing overfitting and promoting better generalization of the model to unseen data (Fig. 8). demonstrates the conversion of the single spectra into a 2D image as was previously explained in (Fig. 6).

4. Results

Ultimately, we proceeded with training our deep learning model with the data. In our model training we carried out three separate protocols.

1. Training the model with the whole data set including spectral data where both hydrogen and methane were present together as well as present separately.
2. Training the model with a limited section of data ONLY containing either hydrogen or methane, as such avoiding the spectral data associated with presence of both gasses at the same time.
3. Increasing the training time of the model in terms of number of epochs of training to explore the potential of model performance with extended training.

4.1. Protocol 1

According to protocol one, the model was trained with 80 % of the total data (hydrogen and methane present together in plasma). The remaining 20 % of the spectral data was kept aside for testing and evaluating the model for its performance assessment after the training.

The model was trained at three stages with an ADAM optimizer algorithm and mean squared error loss function with learning rates of 0.0001 for 200 epochs, followed by a learning rate of 0.00001 for 50 epochs, followed by a learning rate of 0.0000001 for 50 epochs. After training the model was tested with the remaining 20 % of the data which was about 995 spectral readings associated with various hydrogen or methane contents randomly selected during the splitting of the data into train and test section. The results of this protocol are presented in (Fig. 9) where the actual real methane or hydrogen content is in the x axis and the predicted content by the model is presented by the y axis. An ideal perfect prediction should form a perfect straight line when plotting the predicted values against the real values.

While from (Fig. 9), we can see the potential of the model in terms of performing a reasonable regression operation, our objective is to gain maximum accuracy. It seems that at low ppm values for hydrogen and methane the model is struggling to make accurate predictions while it performs better as the gas content increases. We can see that the model is performing significantly better dealing with spectral features associated with methane compared to hydrogen.

4.2. Protocol 2

In this protocol, we trained the model with limited spectral data only associated with presence or absence of either ONLY hydrogen or methane separately (both instance of both gases being present together at the same time in the plasma). In a sense, during this model training, only part of the data associated with only one of these gases being present or absent was used for model training or testing. As before 80 % of the limited data was used for model training and 20 % was used for evaluations. These results are presented in (Fig. 10).

From the results presented in (Fig. 10), we can see significant improvements in terms of model's performance. This indicates that when both gases are present in the plasma simultaneously, the emission peaks associated with the plasma can become more complex and more difficult

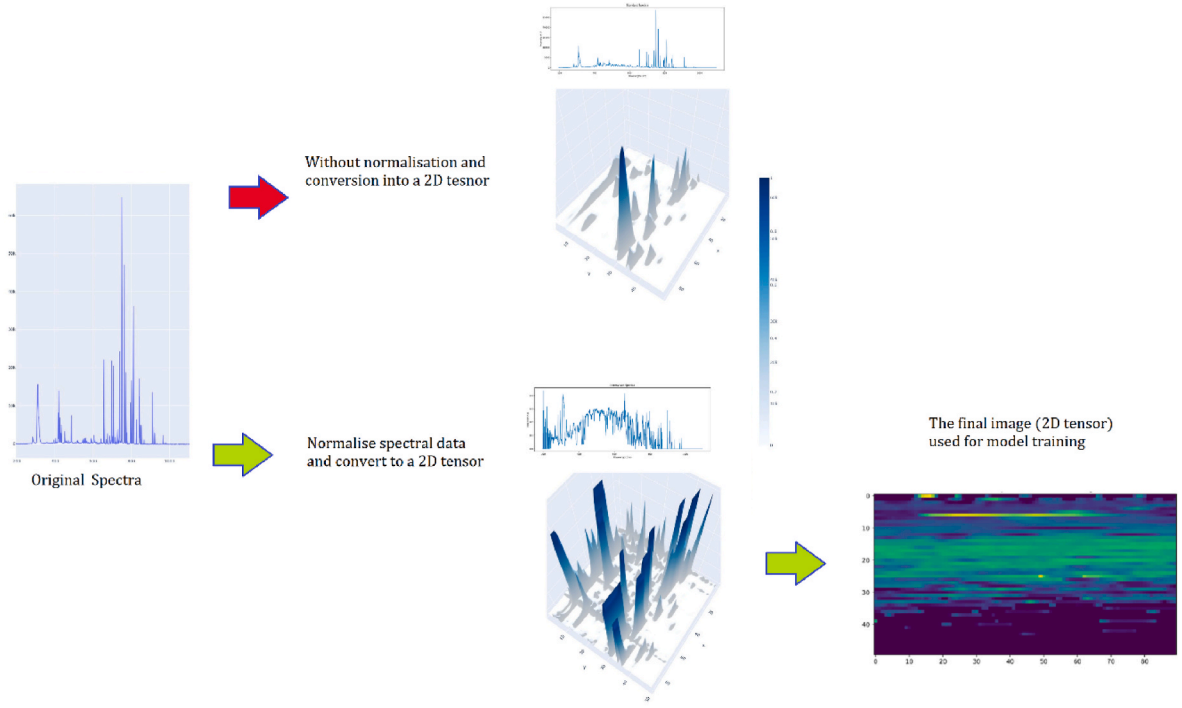

Fig. 8. Steps in converting a spectral data into an image. The spectral data is normalised using min max scaling which leads to a normalised spectral data (green path). The single array spectral data is converted into a matrix with 50 rows and 90 columns. The matrix is then used for training the deep learning model. Without normalising the spectral data (red path), the model was incapable of being trained. (For interpretation of the references to colour in this figure legend, the reader is referred to the Web version of this article.)

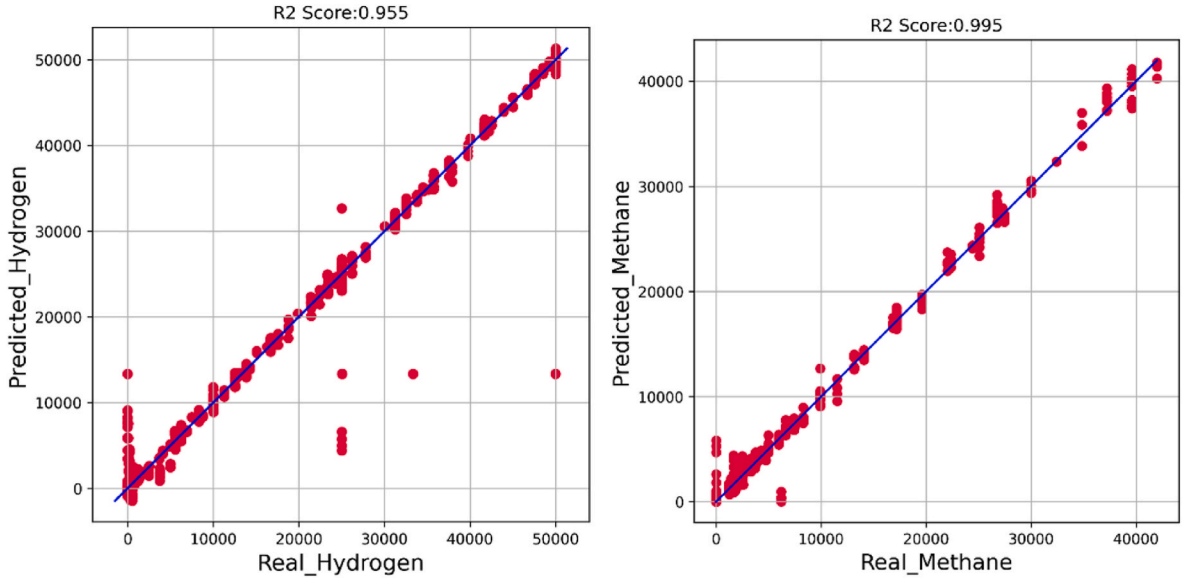

Fig. 9. The trained model was tested with 995 spectral data to predict the hydrogen or methane content of the plasma. The real values associated with ppm content of each gas is presented on the x axis and the model predictions by the y axis.

for the model to train on.

4.3. Protocol 3

Here, protocols one and two were repeated, however with doubling the number of training epochs during model training. After training the model was evaluated with the test data and these results are presented in (Fig. 11 &12).

We can immediately see improvements. However, from the results observed in (Fig. 11), while a significant improvement in methane quantification is observed, the hydrogen quantification by the model almost seems unchanged. This indicates that the extended training has not improved the model in terms of dealing with the spectral data associated with hydrogen presence. However, we can see significant improvement in terms of methane quantification. Especially, we can see improvements in the lower ppm content section.

The results presented in (Fig. 12), indicate that extended training of the model has made significant progress on both hydrogen and methane

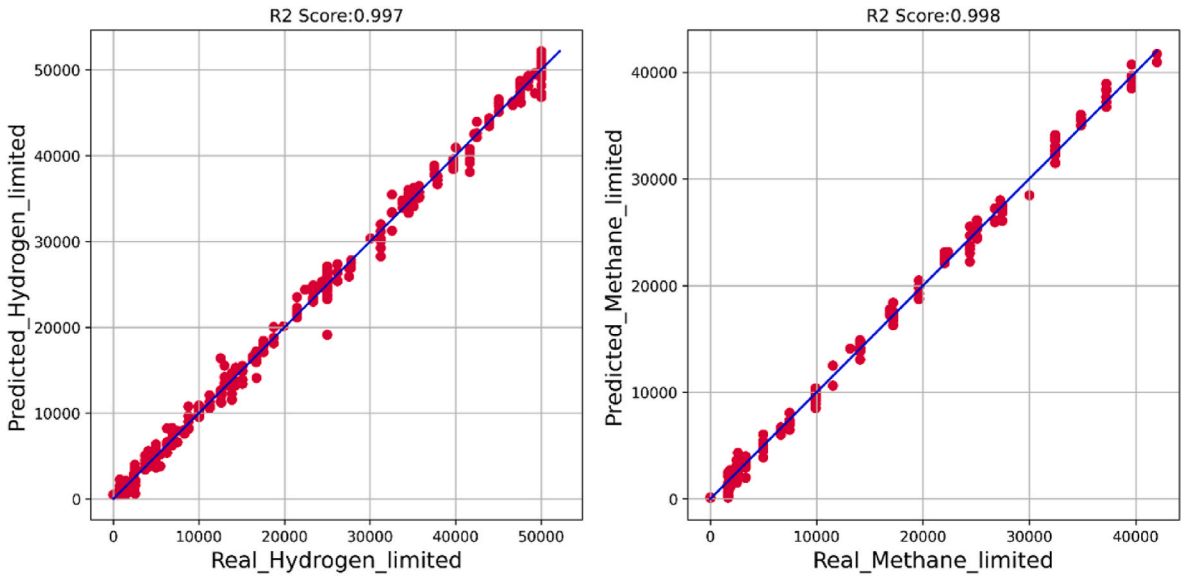

Fig. 10. The performance of the model trained on limited section of the data. With focus on only either hydrogen or methane. The real values associated with ppm content of each gas is presented on the x axis and the model predictions by the y axis.

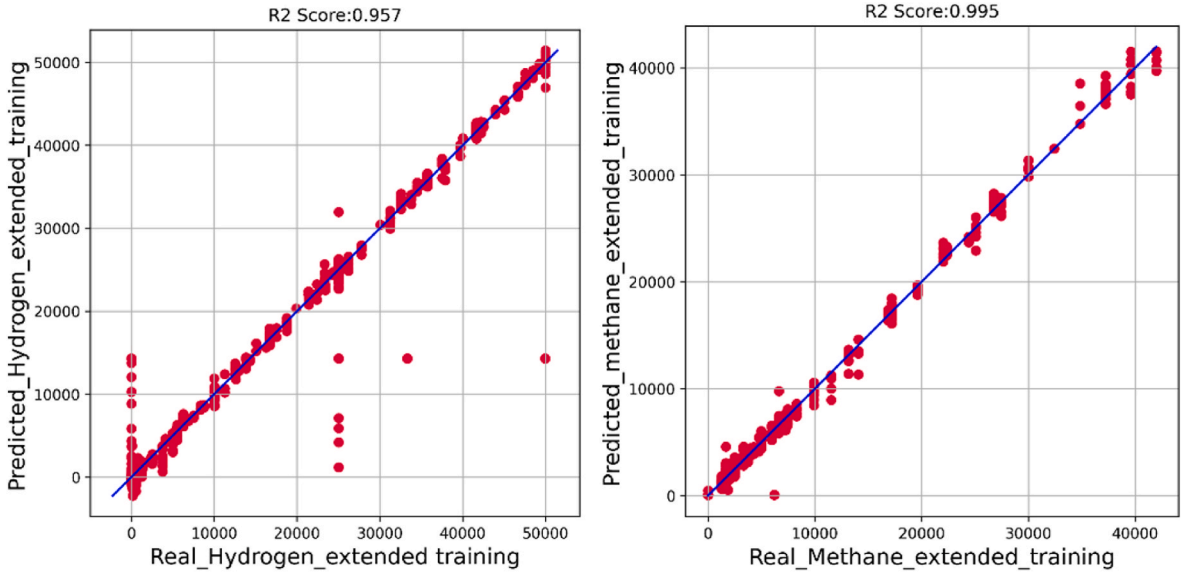

Fig. 11. Model performance on protocol one approach, after significantly extended model training.

quantification. In fact, the methane quantification (prediction) presented in (Fig. 12) is almost resembling a straight line.

5. Discussion

In these experiments, the objective was not to prepare a well-balanced dataset but rather to demonstrate the feasibility of a challenging dataset. The potential of the proposed concept for monitoring the performance of a methane pyrolysis reaction by quantifying methane or hydrogen is evident while significant challenges remain to be addressed. Especially that in a real-world methane hydrolysis process, the output of the process can have other hydrogen containing molecules which will influence the spectral emissions of plasma which will impose significant challenge on the AI model structure and learning curve.

The process of methane pyrolysis can lead to formation of large polycyclic aromatic hydrocarbon (PAH). Methane pyrolysis is in essence the dehydrogenation process of different hydrocarbon compounds to a condensed phase, initiated through rupture of C–H bonds. Higher molecular weight alkene and alkyne particle precursors then form. Acetylene (C2H2), particularly stable at high temperature, appears as a major precursor [57,58].

Tao et al. have addressed the formation of large polycyclic aromatic hydrocarbon. The conclusion of Tao's paper summarizes the key contributions and findings of the study. The authors propose a refined mechanism of C2H2-PAH coupled in a serially connected plug-flow reactor model to address the complex chemical kinetics associated with the formation of seven light-weight EPA-PAHs during acetylene pyrolysis at different temperatures. The mechanism combines kinetic databases from existing mechanisms, incorporating sensitivity analysis and rate-of-production analysis. Missing reactions are added, and rate constants are updated for better predictions of the temperature effect on the formation of two-to four-ring PAHs. The study significantly improves the accuracy of fuel consumption and PAH formation predictions,

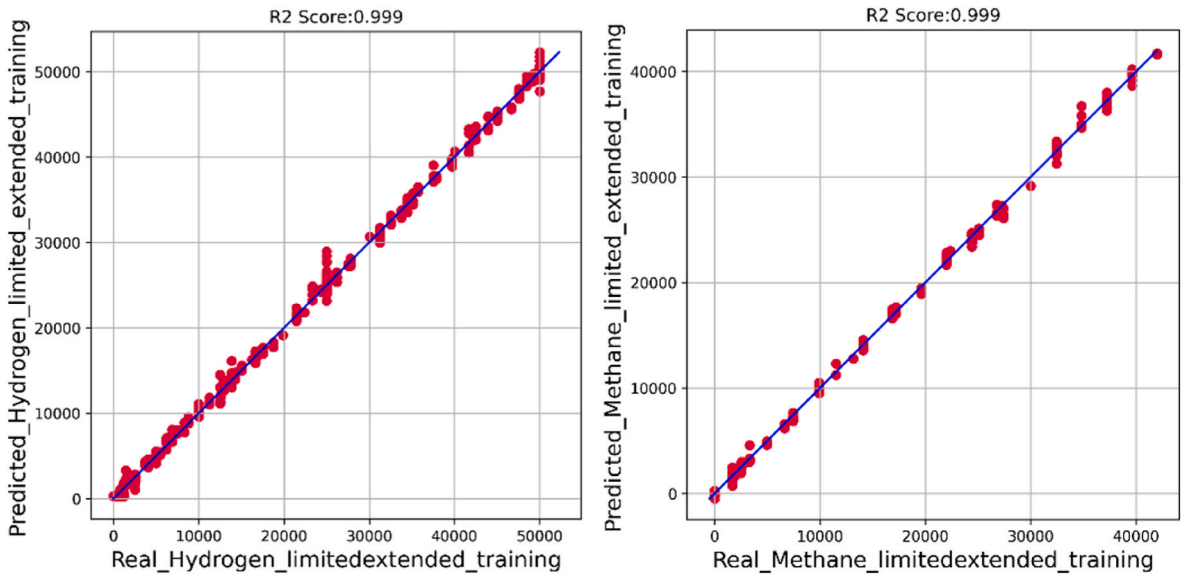

Fig. 12. Model performance on protocol two approach, after significantly extended model training.

achieved through the adoption of a reactor module comprising pre-heating, heat release, and isothermal zones [59].

More recently, Khrabry's proposed model for gas-phase methane pyrolysis represents a significant advancement in understanding the formation of large (PAH) molecules during the synthesis of carbon nanostructures like carbon black and graphene flakes. The model is specifically tailored for studying soot growth kinetics in a two-stage process involving the conversion of methane to acetylene followed by the growth of PAH molecules from acetylene. The chemical mechanism is comprehensive, integrating an older mechanism [60] with key reaction pathways from Tao's mechanism for small (PAH) molecules and incorporating the Hydrogen-Abstraction-C2H2-Addition (HACA) pathways for larger PAH molecules, extending up to 37 aromatic rings.

HACA) mechanism is a chemical reaction pathway involved in the formation of polycyclic aromatic hydrocarbons (PAHs) during high-temperature pyrolysis or combustion of hydrocarbons, particularly acetylene (C2H2). It describes a series of steps in which hydrogen atoms are successively abstracted from acetylene molecules, followed by the addition of the resulting radicals to form larger aromatic hydrocarbons. The HACA mechanism is essential for understanding the complex kinetics of PAH formation, as it provides insights into the molecular pathways leading to the growth of aromatic structures. These mechanisms play a crucial role in various high-temperature processes, such as flames, soot formation, and pyrolysis reactions, where the formation of PAHs is of interest [61].

This approach allows the model to accurately describe both stages of methane pyrolysis. The mechanism's validity is confirmed through comparisons with multiple sets of experimental data, demonstrating good agreement for both conversion processes. The model's performance is evaluated in methane-rich mixtures under extended residence times, emphasizing the importance of including larger PAH species (up to A37) for precise predictions of carbon conversion to PAH molecules and the residual fraction of acetylene in the mixture. The mechanism file's availability upon request highlights its potential for contributing to further research in the field. Khrabry's model provides a valuable tool for researchers studying methane pyrolysis and the synthesis of carbon nanostructures [62].

As such, it is apparent that these studies ultimately need to be carried out with a variety of input gases into the plasma, capturing spectral data followed by extensive model training and evaluating model's performance metrics to conclude the method applicable for commercial consideration.

Apart from the above-mentioned extensive studies required as a follow up on what has been reported here, our proposed system, in its current early stage, requires significant improvements. Most notably, as evident from the results, in a conceptual scenario depicted in (Fig. 2), the system would dilute a small sample stream of hydrogen product and assess it for the presence of methane. In an ideal methane hydrolysis reaction, the goal would be to convert 100 % of methane into hydrogen. Therefore, the system should ideally be capable of quantifying even trace amounts of methane. This necessitates quantifying methane at very low levels, such as parts per million (ppm) or billion quantities. While the results in (Fig. 11) associated with methane quantification show promise, achieving significantly higher accuracy is essential. We should aim for quantification accuracy close to what was observed in (Fig. 12) in relation to methane. At the same time, due to the early stage of our experiments and resource limitations, the lowest methane dilution tested was approximately 1230 ppm, which may be considered relatively high. A hydrogen tank containing 1200 ppm of methane would still be considered 99.87 % pure. To achieve purities in the range of 99.999 % or 99.99 %, the methane impurity should ideally be between 1 and 100 ppm. While we have demonstrated the great potential of this concept 's approach at its early stage, ongoing studies should continue to assess the precision and performance of the concept.

One observation in our results that presents a challenge is the quantification of hydrogen in the presence of methane (in this study) and other hydrogen bearing molecules (in future studies). When comparing the results associated with hydrogen quantification in (Figs. 9 and 11), extended model training failed to make a significant improvement to the model's learning. These results pertain to quantifying hydrogen in the presence of methane. Methane, containing four hydrogen atoms, can potentially break into small molecular or atomic fragments when placed in a plasma, technically yielding hydrogen atoms. And extensive amount of research exists on decomposition of methane via plasma and the molecular break down of methane into various ions, radical or neutrals [63–67]. The presence of hydrogen, specially at low concentrations is impossible to be recognised by the naked eye as illustrated in (Fig. 13) compared to the elaborated effect of methane presence.

According to the literature, the following reactions can cooccur when methane is exposed to the plasma environment [66].

$$CH4 + e \rightarrow CH3\bullet + H\bullet + e$$

$$CH4 + e \rightarrow CH4^{+} + 2e$$

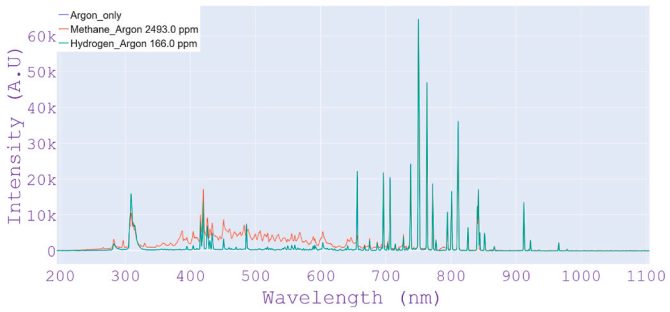

Fig. 13. The standard spectral data associated with plasma emissions lacking or containing the stated amount of hydrogen or methane. The presence of methane results in significant alternation of the spectrum between 300 and 700 nm while the presence of hydrogen is impossible to be observed with naked eye. The subtle differences in these spectra, challenging to distinguish with the naked eye, underscore the exceptional sensitivity of our computer vision-based models. Further insights into this remarkable capability will be provided in the revised version, showcasing the precision of our methodology in capturing nuanced variations in gas composition.

$CH4^+ + CH4 \rightarrow CH5^+ + CH3\bullet$

$CH5^+ + C2H6 \rightarrow C2H5^+ + CH4 + H2$

$CH5^+ + C2H4 \rightarrow C2H5^+ + CH4$

$C2H5+ + C2H6 \rightarrow C3H7+ + CH4$

$C2H5+ + C2H6+CH4 \rightarrow C4H9+ + H2 + CH4$

In each of the above reactions, the rate and efficiency of every individual conversion is dependent on the ration of the inert gas and the methane present in the plasma, the flow rates of the gases, the plasma power and chamber dynamics.

This is further illustrated in (Fig. 14) where the three spectra data presented earlier in (Fig. 13) are converted in to 2D tensors and the intensity associated with the emission peaks is projected in the z axis.

For example, molecules such as intermediate methanium ($C2H5^+$) formation and subsequently its own further reaction with a methane molecule in the plasma has its own dependencies compared to an earlier reaction or a further reaction [66]. Atomic and molecular hydrogen ions also have been observed in these studies. The methane conversion and electron density/energy have been shown to be correlated while the electron density and energy will impact further ion formation and govern the stability of the plasma [67]. In fact, this topic is so extensively vast for discussion that it will be beyond the scope of this article. However, one observation is mostly important in relation to the topic of this article, and that is the formation of varying amount of hydrogen when the methane is exposed to the plasma. This simply means that in all the experiments where we introduce 'only' methane and argon into the plasma, there will be hydrogen present in there. But when we are training our neural network model, according to our experimental input, our model assumes hydrogen not to exists in there. But spectral signals associated with hydrogen exist. So, the model is literally getting trained with a small dose of wrong information in relation to hydrogen content.

Consequently, when spectral data is captured with a known flow rate of hydrogen into the plasma, there is an unknown quantity of hydrogen that may appear in the plasma when methane is present, leading to an error factor. Spectral peaks associated with hydrogen are limited and unique, whereas methane can exhibit significantly more complex spectral features. This creates a potential challenge for the deep learning model because, during training, we provide a known quantity of

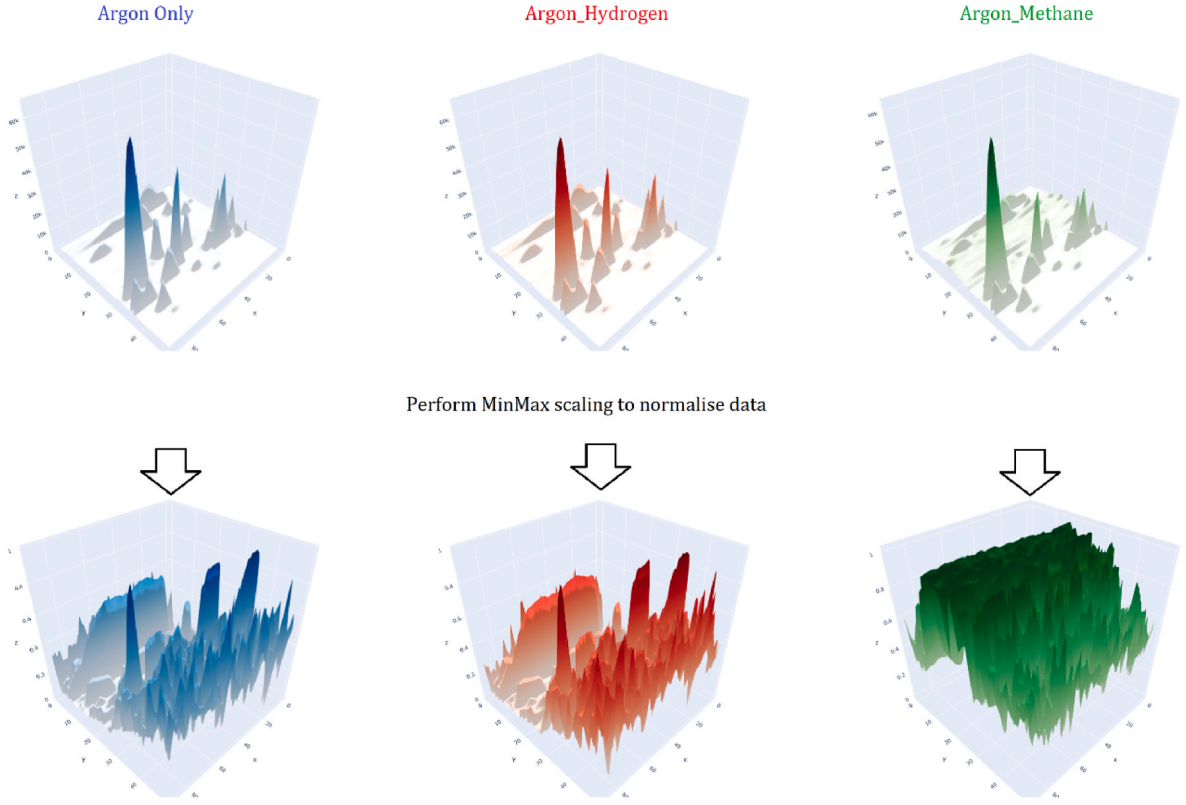

Fig. 14. Visualising the 2D tensors generated from the spectral data such that the intensity of each pixel in the 2D tensor is projected in z axis. Top row represents spectral data prior to normalization and the bottom row represents the spectral data after normalization via min max scaling. The bottom row images represent what the deep learning model is ultimately getting trained on for feature identification. The presence of methane clearly generates an image which is significantly more distinguishable than the one with hydrogen presence.

hydrogen to the AI model while simultaneously depriving it of the quantity of hydrogen that may arise from the presence of methane in the plasma. Consequently, the model is trained with an error in its learning curve. This can be observed in (Figs. 9 and 11), especially when considering the hydrogen content values predicted by the model (up to 15,000 ppm), while the real values for the hydrogen content fed into the plasma were 0. While further training of the model resolves this issue for methane, it fails to do so for hydrogen quantification.

5.1. The required improvements should be pursued through two parallel approaches

Further enhancement of hardware: This refers to the plasma unit system. Many parameters in this hardware, such as the chamber size, plasma generator, plasma power, plasma pulse rate, chamber pressure controls, mass flow controller sensitivity, and collimator optics capturing plasma emissions, can be explored, and tested to achieve better performance.

Further improvements in the neural network model: There is virtually no limit to what can be achieved in terms of neural network model improvements. Current advancements in deep learning and computer vision models offer exciting possibilities. While our experiments used a model resembling ResNet50, which is powerful but not the latest, many more sophisticated models are being developed by computer vision and AI scientists. Future iterations of this project can significantly benefit from implementing these advancements in AI and computer vision. The results presented in (Figs. 9–12). illustrate that even extending the model training epoch by a factor of two led to significant improvements. Therefore, it's reasonable to assume that employing more updated and sophisticated computer vision models will guarantee further enhancements.

6. Conclusion

In this study, our primary objective was to explore the feasibility of integrating plasma analysis and deep learning to precisely quantify a specific set of molecules, namely hydrogen and methane, hypothetically resulting from methane pyrolysis reactions. While the developed model exhibits robust performance in quantifying this limited set of elements, it faces inherent challenges in accurately quantifying a broader spectrum of hydrogen-bearing molecules potentially present in the pyrolysis output. Despite showcasing promising outcomes, it is crucial to acknowledge the necessity of experimental setups that involve a diverse range of gases, facilitating spectral data capture for extensive model training. Recognizing the dynamism in deep learning advancements, the study emphasizes the potential of deploying sophisticated and complex models to overcome these challenges. Consequently, the project, in its current nascent stage, serves as a trailblazing endeavour, illustrating the convergence of plasma analysis, AI, and deep learning within the realm of industrial applications, particularly in the context of methane pyrolysis. This multidisciplinary approach not only highlights the current achievements but also underscores the immense research opportunities lying ahead.

Declaration of competing interest

The authors declare that they have no known competing financial interests or personal relationships that could have appeared to influence the work reported in this paper.

Acknowledgments

This project has been internally funded by London Southbank University (LSBU) and the authors would like to thank prof Tara Dean at LSBU for her support on this project.

References

[1] Viswanathan B. Hydrogen as an energy carrier. In: Energy sources: fundamentals of chemical conversion processes and applications. Elsevier Science BV; 2017.
[2] Abbas HF, Daud WMAW. Hydrogen production by methane decomposition: a review. Int J Hydrogen Energy 2010;35(3):1160–90.
[3] Karchiyappan T. A review on hydrogen energy production from electrochemical system: benefits and challenges. Energy Sources, Part A 2019;41(7):902–9.
[4] Younessi-Sinaki M, Matida EA, Hamdullahpur F. Kinetic model of homogeneous thermal decomposition of methane and ethane. Int J Hydrogen Energy 2009;34(9):3710–6.
[5] Zhang JB, Li X, Xie WT, Hao QQ, Chen HY, Ma XX. K2CO3-promoted methane pyrolysis on nickel/coal-char hybrids. J Anal Appl Pyrol 2018;136:53–61.
[6] Weger L, Abánades A, Butler T. Methane cracking as a bridge technology to the hydrogen economy. Int J Hydrogen Energy 2017;42(1):720–31.
[7] Machhammer O, Bode A, Hormuth W. Financial and ecological evaluation of hydrogen production processes on a large scale. Chem Eng Technol 2016;39(6):1185–93.
[8] Shu DY, Deutz S, Winter BA, Baumgärtner N, Leenders L, Bardow A. The role of carbon capture and storage to achieve net-zero energy systems: trade-offs between economics and the environment. Renew Sustain Energy Rev 2023;178:113246.
[9] Von Wald GA, Masnadi MS, Upham DC, Brandt AR. Optimization-based technoeconomic analysis of molten-media methane pyrolysis for reducing industrial sector CO2 emissions. Sustain Energy Fuels 2020;4(9):4598–613.
[10] Li Y, Zhang T, Ma J, Deng X, Gu J, Yang F, Ouyang M. Study the effect of lye flow rate, temperature, system pressure, and different current density on energy consumption in catalyst test and 500W commercial alkaline water electrolysis. Mater Today Phys 2022;22:100606.
[11] Parkinson B, Tabatabaei M, Upham DC, Ballinger B, Greig C, Smart S, McFarland E. Hydrogen production using methane: techno-economics of decarbonizing fuels and chemicals. Int J Hydrogen Energy 2018;43(5):2540–55.
[12] Harikrishna RB, Sharma S, Deka H, Sundararajan T, Rao GR. Thermochemical production of green hydrogen using ferrous scrap materials. Int J Hydrogen Energy 2023.
[13] Steinberg M. Fossil fuel decarbonization technology for mitigating global warming. Int J Hydrogen Energy 1999;24(8):771–7.
[14] Dai H, Besser RS. Fluidization analysis for catalytic decomposition of methane over carbon blacks for solar hydrogen production. Int J Hydrogen Energy 2021;46(79):39079–94.
[15] Keller M. Comment on 'methane pyrolysis for zero-emission hydrogen production: a potential bridge technology from fossil fuels to a renewable and sustainable hydrogen economy. Ind Eng Chem Res 2021;60(48):17792–4.
[16] Parkinson B, Balcombe P, Speirs JF, Hawkes AD, Hellgardt K. Levelized cost of CO2 mitigation from hydrogen production routes. Energy Environ Sci 2019;12(1):19–40.
[17] Sanchez-Bastardo N, Schlogl R, Ruland H. Methane pyrolysis for CO2-free H2 production: a green process to overcome renewable energies' unsteadiness. Chem Ing Tech 2020;92(10):1596–609.
[18] Shah N, Panjala D, Huffman GP. Hydrogen production by catalytic decomposition of methane. Energy Fuels 2001;15(6):1528–34.
[19] Bayat N, Rezaei M, Meshkani F. Hydrogen and carbon nanofibers synthesis by methane decomposition over Ni–Pd/Al2O3 catalyst. Int J Hydrogen Energy 2016;41(12):5494–503.
[20] Bayat N, Rezaei M, Meshkani F. Methane decomposition over Ni–Fe/Al2O3 catalysts for production of CO2-free hydrogen and carbon nanofiber. Int J Hydrogen Energy 2016;41(3):1574–84.
[21] Ashik UPM, Wan Daud WMA, Abbas HF. Production of greenhouse gas-free hydrogen by thermocatalytic decomposition of methane - a review. Renew Sustain Energy Rev 2015;44:221–56.
[22] Pudukudy M, Yaakob Z, Jia Q, Sobri Takriff M. Catalytic decomposition of undiluted methane into hydrogen and carbon nanotubes over Pt promoted Ni/CeO2 catalysts. New J Chem 2018;42(18):14843–56.
[23] Plevan M, et al. Thermal cracking of methane in a liquid metal bubble column reactor: experiments and kinetic analysis. Int J Hydrogen Energy 2015;40(25):8020–33.
[24] Geißler T, et al. Hydrogen production via methane pyrolysis in a liquid metal bubble column reactor with a packed bed. Chem Eng J 2016;299:192–200.
[25] Palmer C, et al. Methane pyrolysis with a molten Cu–Bi alloy catalyst. ACS Catal 2019;9(9):8337–45.
[26] Chester UD, et al. Catalytic molten metals for the direct conversion of methane to hydrogen and separable carbon. Science 2017;358(6365):917–21.
[27] Serban M, Lewis MA, Marshall CL, Doctor RD. Hydrogen production by direct contact pyrolysis of natural gas. Energy Fuels 2003;17(3):705–13.
[28] Rahimi N, et al. Solid carbon production and recovery from high-temperature methane pyrolysis in bubble columns containing molten metals and molten salts. Carbon 2019;151:181–91.
[29] Kang D, et al. Catalytic methane pyrolysis in molten MnCl2-KCl. Appl Catal B Environ 2019;254:659–66.
[30] Kang D, et al. Catalytic methane pyrolysis in molten alkali chloride salts containing iron. 2020.
[31] Nnabuife SG, Ugbeh-Johnson J, Okeke NE, Ogbonnaya C. Present and projected developments in hydrogen production: a technological review. Carbon Capture, Sci Technol 2022;3:100042.
[32] Reddy Patlolla Shashank, Katsu Kyle, Sharafian Amir, Wei Kevin, Herrera Omar E, Walter Mérida. A review of methane pyrolysis technologies for hydrogen production. Renew Sustain Energy Rev 2023;181:113323.

[33] Sánchez-Bastardo Nuria, Schlögl Robert, Ruland Holger. Methane pyrolysis for zero-emission hydrogen production: a potential bridge technology from fossil fuels to a renewable and sustainable hydrogen economy. Ind Eng Chem Res 2021;60 (32):11855–81.
[34] Zheng C, Ye W, Sanchez NP, Li C, Dong L, Wang Y, Griffin RJ, Tittel FK. Development and field deployment of a mid-infrared methane sensor without pressure control using interband cascade laser absorption spectroscopy. Sensor Actuator B Chem 2017;244:365–72.
[35] Zhang JY, Ding EJ, Xu SC, Wang XX, Song F. Sensitization of an optical fiber methane sensor with graphene. Opt Fiber Technol 2017;37:26–9.
[36] Tombez L, Zhang EJ, Orcutt JS, Kamlapurkar S, Green WMJ. Methane absorption spectroscopy on a silicon photonic chip. Optica 2017;4:1322.
[37] Campanella CE, de Carlo M, Cuccovillo A, de Leonardis F, Passaro VMN. Methane gas photonic sensor based on resonant coupled cavities. Sensors 2019;19:5171.
[38] Bíró F, Dücső C, Radnóczi GZ, Baji Z, Takács M, Bársony I. ALD nano-catalyst for micro-calorimetric detection of hydrocarbons. Sensor Actuator B Chem 2017;247: 617–25.
[39] Alpert B, Ferri E, Bennett D. Algorithms for identification of nearly-coincident events in calorimetric sensors. J Low Temp Phys 2016;184:263–73.
[40] Shen G, Zheng X, Zhang Y, Wang R. The designed MEMS methane sensor based on pulse power supply. IOP Conf Ser Earth Environ Sci 2019;300:42029.
[41] Gardner EL, Luca AD, Falco C, Udrea F. Geometrical optimization of diode-based calorimetric thermal flow sensors through multiphysics finite element modeling. Proceedings 2017;1:280.
[42] Hu L, Zheng C, Zhang M, Yao D, Zheng J, Zhang Y, Wang Y, Tittel FK. Quartz-enhanced photoacoustic spectroscopic methane sensor system using a quartz tuning fork-embedded, double-pass and off-beam configuration. Photoacoustics 2020;18:100174.
[43] Liu H, He Q, Zheng C, Wang Y. Development of a portable mid-infrared methane detection device. Optoelectron Lett 2017;13:100–3.
[44] Dong M, Zheng C, Miao S, Zhang Y, Du Q, Wang Y, Tittel F. Development and measurements of a mid-infrared multi-gas sensor system for CO, CO2 and CH4 detection. Sensors 2017;17:2221.
[45] Moalaghi M, Gharesi M, Ranjkesh A, Hossein-Babaei F. Tin oxide gas sensor on tin oxide microheater for high-temperature methane sensing. Mater Lett 2019;263: 127196.
[46] Shaalan NM, Rashad M, Moharram AH, Abdel-Rahim MA. Promising methane gas sensor synthesized by microwave-assisted Co3O4 nanoparticles. Mater Sci Semicond Process 2016;46:1–5.
[47] Oleksenko LP, Fedorenko GV, Maksymovych NP. Platinum-containing adsorption-semiconductor sensors based on nanosized tin dioxide for methane detection. Theor Exp Chem 2017;53:259–64.
[48] Oleksenko LP, Fedorenko GV, Maksymovych NP. Highly sensitive to methane sensor materials based on Nano-Pd/SnO2. Theor Exp Chem 2019;55:1–5.
[49] Wan H, Yin H, Lin L, Zeng X, Mason AJ. Miniaturized planar room temperature ionic liquid electrochemical gas sensor for rapid multiple gas pollutants monitoring. Sensor Actuator B Chem 2018;255:638–46.
[50] Yang B, Xu J, Wang C, Xiao J. A potentiometric sensor based on SmMn2O5 sensing electrode for methane detection. Mater Chem Phys 2020;245:122679.
[51] Gross PA, Jaramillo T, Pruitt B. Cyclic-voltammetry-based solid-state gas sensor for methane and other VOC detection. Anal Chem 2018;90:6102–8.
[52] Liu X, et al. Establishment of analysis method for methane detection by gas chromatography. IOP Conf Ser Earth Environ Sci 2018;113:012023.
[53] Vincent J, et al. Detecting trace methane levels with plasma optical emission spectroscopy and supervised machine learning. Plasma Sources Sci Technol 2020; 29:085018.
[54] He K, Zhang X, Ren S, Sun J. Deep residual learning for image recognition. In: Proceedings of the IEEE conference on computer vision and pattern recognition (CVPR), Las Vegas, NV, USA, 27–30 june 2016; 2016. p. 770–8.
[55] Cornell University Computational Optimization Open Textbook. (n.d.). Optimization in machine learning and data analytics. Retrieved August 28, 2023, from https://optimization.cbe.cornell.edu/index.php?title=Adam.
[56] Kingma DP, Ba J. Adam: a method for stochastic optimization. In: 3rd international conference on learning representations; 2014.
[57] Fulcheri L, Rohani V-J, Wyse E, Hardman N, Dames E. An energy-efficient plasma methane pyrolysis process for high yields of carbon black and hydrogen. Int J Hydrogen Energy 2023;48(8):2920–8.
[58] Frenklach M, Clary DW, Gardiner WC, Stein SE. Detailed kinetic modeling of soot formation in shock-tube pyrolysis of acetylene. Symp (Int) Combust 1985;20(1): 887–901.
[59] Tao H, Wang HY, Ren W, Lin KC. Kinetic mechanism for modelling the temperature effect on PAH formation in pyrolysis of acetylene. Fuel 2019;255:115796.
[60] Appel J, Bockhorn H, Frenklach M. Kinetic modeling of soot formation with detailed chemistry and physics: laminar premixed flames of C2 hydrocarbons. Combust Flame 2000;121(1–2):122–36.
[61] Mebel AM, Georgievskii Y, Jasper AW, Klippenstein SJ. Temperature- and pressure-dependent rate coefficients for the HACA pathways from benzene to naphthalene. Proc Combust Inst 2017;36(1):919–26.
[62] Khrabry A, Kaganovich ID, Barsukov Y, Raman S, Turkoz E, Graves D. Compact and accurate chemical mechanism for methane pyrolysis with PAH growth. Int J Hydrogen Energy 2024;56:1340–60.
[63] Sugai H, Kojima H, Ishida A, Toyoda H. Spatial distribution of CH3 and CH2 radicals in a methane rf discharge. Appl Phys Lett 1990;56(26):2616–8. 25 June 1990.
[64] Tachibana K, Nishida M, Harima H, Urano Y. Diagnostics and modeling of a methane plasma used in the chemical vapor deposition of amorphous carbon films. J Phys Appl Phys 1984;17(8):1727.
[65] Sun J, Chen Q. Kinetic roles of vibrational excitation in RF plasma assisted methane pyrolysis. J Energy Chem 2019;39:188–97.
[66] Bae J, Lee M, Park S, Jeong M-G, Hong D-Y, Kim YD, Park Y-K, Hwang YK. Investigation of intermediates in non-oxidative coupling of methane by non-thermal RF plasma. Catal Today 2017;293–294:105–12.
[67] Sun H, Katayama K, Oya M. Contribution of electron density to plasma decomposition rate of methane. Fusion Eng Des 2023;194:113885.